

# RSC Advances



This is an *Accepted Manuscript*, which has been through the Royal Society of Chemistry peer review process and has been accepted for publication.

*Accepted Manuscripts* are published online shortly after acceptance, before technical editing, formatting and proof reading. Using this free service, authors can make their results available to the community, in citable form, before we publish the edited article. This *Accepted Manuscript* will be replaced by the edited, formatted and paginated article as soon as this is available.

You can find more information about *Accepted Manuscripts* in the [Information for Authors](#).

Please note that technical editing may introduce minor changes to the text and/or graphics, which may alter content. The journal's standard [Terms & Conditions](#) and the [Ethical guidelines](#) still apply. In no event shall the Royal Society of Chemistry be held responsible for any errors or omissions in this *Accepted Manuscript* or any consequences arising from the use of any information it contains.

# Fe (III) induced structural, optical, and dielectric behavior of cetyltrimethyl ammonium bromide stabilized strontium stannate nanoparticles synthesized by facile wet chemistry route

*Astakala Anil Kumar<sup>1</sup>, Ashok Kumar<sup>1,\*</sup>, J. K. Quamara<sup>1</sup>, G. R. Dillip<sup>2</sup>, Sang Woo Joo<sup>2</sup> and Jitendra Kumar<sup>3</sup>*

*<sup>1</sup>Department of Physics, National Institute of Technology Kurukshetra, Haryana 136119, INDIA*

*\*Email: ashokku@nitkkr.ac.in, Tel: +91-1744133498*

*<sup>2</sup>School of Mechanical Engineering and Technology, Yeungnam University, Gyeongsan, 712-749, South Korea*

*<sup>3</sup>Materials Science Programme, Indian Institute of Technology Kanpur, 208016, INDIA*

**Abstract:** We report synthesis of Fe containing strontium stannate (SrSnO<sub>3</sub>) nanoparticles by facile cost-effective wet chemistry route using cetyltrimethyl ammonium bromide (CTAB) as surfactant. Thermogravimetric analysis together with differential scanning calorimetric data revealed the formation of initial compound as SrSn(OH)<sub>6</sub>, which led to the formation of SrSnO<sub>3</sub> via three main endothermic dehydration cycles. The X-ray diffraction patterns of final compound revealed the formation of orthorhombic phase of SrSnO<sub>3</sub> with Pbnm symmetry, and exhibited contraction of cell volume with increase in Fe content. Raman spectra showed the peaks at 220, 256, 306, 404, 452 and 561 cm<sup>-1</sup> corresponding to Sn-O and O-Sn-O band stretching. The band gap values were found as 4.17, 3.81 and 3.52 eV, respectively for the samples with 0, 2 and 4 at % Fe content. The photoluminescence spectra also confirmed the red shift of band emission peak observed around 370 nm. The relative permittivity was observed to be low and showed steady variation with temperature and Fe content. The dielectric relaxation time was found to decrease with temperature and increase with Fe content. The ac conductivity values were 3.23 x 10<sup>-8</sup>, 3.98 x 10<sup>-8</sup> and 4.47 x 10<sup>-8</sup> Ω<sup>-1</sup> cm<sup>-1</sup>, and activation energy was found to be 0.22, 0.34 and 0.44 eV for for pristine and Fe (2 and 4 at %), respectively. Conductivity analysis suggests that the hopping of charge carriers in the crystal as the possible mechanism for electric conduction.

## 1. Introduction

Among the perovskite, alkaline earth stannates ( $\text{MSnO}_3$ ,  $M = \text{Mg, Ca, Sr, Ba}$ ) form a special class of materials due to their structural, optical, dielectric properties and photovoltaic behavior [1-4]. These properties have been tailored by substituting host cations by transition metal ions [5, 6]. The alkaline earth stannates falls in the class of ferroelectric oxides, that are used in the fabrication of electronic components in various electronic devices such as capacitors, thermistors and transducers as they are having low temperature coefficient of capacitance [7]. Particularly, strontium stannate ( $\text{SrSnO}_3$ ) is a wide band gap ( $\sim 4.1$  eV) direct semiconductor and having high resistance at room temperature, in order to enhance the conductivity of these semiconductors it is necessary to dope them with an external atom at the cationic site [8, 9]. The perovskite structured strontium stannate nanoparticles are found to possess steady variation of capacitance with temperature [10]. As the technology advances, the need of electronic components which operates at higher frequency and having steady variance of capacitance with temperature at higher frequency is required to store and transfer of large volume of information. This makes the component fabricated by using these materials to exploit extensively in telecommunications and radio applications [11,12]. As these materials are having potential applications in the fabrication of electronic devices, synthesis of their low dimensional structures is crucial. The perovskite structured strontium stannate nanoparticles have been synthesized through various techniques such as co-precipitation, solid state reaction, hydrothermal and sol-gel wet chemistry route [13-16]. The sol-gel is one of the promising cost effective techniques to synthesize nanoparticles and gives considerably high yield of the final product at low decomposition temperatures [17]. Several dopants such as La, Er, Fe and Co have been used to engineer the behavior of  $\text{SrSnO}_3$  [18,19]. It was reported that the dielectric and conducting behavior of  $\text{SrSnO}_3$  has been enhanced by substitution of the host cations with rare earth metal ions [20]. However, the relaxation behavior of Sr substitution in the  $\text{SrSnO}_3$  by Fe has not been studied yet. Further, as structural changes in a system affects the physical and optical properties, a detail study of dielectric and allied properties of Fe substituted strontium stannate assumed to have greater significance in order to have a complete picture on dielectric behavior of wideband gap strontium stannate nanoparticles. There are few reports available on optical and conductivity behavior of  $\text{SrSnO}_3$  nanoparticles with different transition metal ion substitution [21,22]. Moreover, the dielectric relaxation of transition metal ion doped  $\text{SrSnO}_3$  is

not yet studied. The present paper provides a correlation between structural, optical and dielectric behavior of the pristine and Fe doped perovskite  $\text{SrSnO}_3$  nanoparticles synthesized by facile wet chemistry route, which were stabilized by cetyltrimethyl ammonium bromide (CTAB).

## 2. Experimental

The Fe substituted strontium stannate nanoparticles with general formula  $\text{SrSn}_{1-x}\text{Fe}_x\text{O}_{3-\delta}$  ( $0 \leq x \leq 0.04$ ) have been synthesized by facile cost-effective wet chemistry route using cetyltrimethyl ammonium bromide (CTAB) as a surfactant. The presence of the surfactant can alter the surface energy of the crystal surfaces and promotes the anisotropic growth of nanoparticles. In the present work CTAB used as a surfactant which plays a major role in monodispersion of the synthesized nanoparticles which is illustrated in the Scheme 1. First, the aqueous solution of tin chloride ( $\text{SnCl}_2 \cdot 2\text{H}_2\text{O}$ ) and ferric nitrate  $\text{Fe}(\text{NO}_3)_3 \cdot 9\text{H}_2\text{O}$  was obtained and subsequently the former solution was added drop wise with the aqueous solution of strontium nitrate ( $\text{Sr}(\text{NO}_3)_2$ ). Afterward, the CTAB with maintaining the 0.03 mM concentration in final solution was added to the above solution. The resulting solution was stirred at  $80^\circ\text{C}$  for 4 h to obtain the gel, followed by drying at  $100^\circ\text{C}$  for 2 h and these powders were washed several times with ethanol to remove surface impurities and polymer present in the compound. These dried powders were calcined at  $650^\circ\text{C}$  for 2 h to obtain the Fe (0, 2, 4 at.%) doped  $\text{SrSnO}_3$  nanoparticles. The diagram for the synthesis of  $\text{SrSnO}_3$  nanoparticles is given in Scheme 1. Thermogravimetric analysis (TG) and differential scanning calorimetry (DSC) was performed collectively by using SDT-Q600 Thermal Analyser. The DSC-TG analysis was performed in the nitrogen atmosphere at the heating rate of 5 K/min. The phase(s) of the synthesized perovskite pristine and Fe (2 and 4 at.%)  $\text{SrSnO}_3$  nanoparticles were analyzed by using PAN analytical X'pert pro X-ray diffractometer using  $\text{CuK}_\alpha$  radiation ( $\lambda = 1.541874\text{\AA}$ ,  $K_{\alpha 1}/K_{\alpha 2}:: 2/1$ ) at 40 kV and 30 mA. The data recorded over a  $2\theta$  range of  $20-80^\circ$  with step size as  $0.03^\circ/\text{min}$ . Morphological characterization of as-synthesized samples was performed by using transmission electron microscopy (Tecnai G2 F20 S-Twin) with an accelerating voltage of 200 kV. Raman spectra were collected using LABRAM HR 800 micro Raman spectrometer in the range of  $150-800\text{ cm}^{-1}$  using a solid state laser with wavelength of 633 nm. Diffuse reflectance spectra of powders in solid state were recorded by UV-Visible spectrometer, PG instruments Pvt. Ltd. T90+ in the spectral range of 230-700 nm.

Photoluminescence spectra were collected in the wavelength range of 320 - 550 nm with the excitation wavelength of 290 nm using Simadzu RF-530 spectrofluorometer. X-ray photoelectron spectra (XPS) was recorded with Thermo Scientific K-alpha X-ray photoelectron spectrometer having a monochromatic Al-K $\alpha$  source. The impedance analysis at different temperatures was performed using Aglient E 4980A, Precision LCR Meter in the frequency range between 20 Hz to 2 MHz.

### 3. Results and discussion

#### 3.1 Structural and phase analysis

Fig. 1(a) shows the variation of the weight (of the powder obtained after drying the gel at 100 °C) in the nitrogen atmosphere as the function of temperature in the range of 300-1200 K at a heating rate of 5 K/min. The three stages of weight loss are clearly visible. The first stage (~300 – 410 K) is observed to be faster as compared to the second (~410-720 K) and third (~720 – 840 K) stages. However, the third stage which takes place via one fast and one slow dehydration steps reveals the fastest water removal rate in its first half cycle. The initial compound obtained after drying the gel is assumed to be SrSn(OH)<sub>6</sub>, and the intermediate products formed in all the three stages as per weight estimates are assumed as SrSnO(OH)<sub>4</sub>, and SrSnO<sub>2</sub>(OH)<sub>2</sub>, respectively. The weight loss is found to be approximately 6.4 %, 6.2 % and 6.1 %, respectively (for all the observed three stages) and is matching well with the theoretical estimates. In the first stage, the weight loss is observed to be in three steps with intermediate products formed to be as SrSnO(OH)<sub>4</sub>. 2/3 H<sub>2</sub>O, SrSnO(OH)<sub>4</sub>.1/3 H<sub>2</sub>O and SrSnO(OH)<sub>4</sub>, respectively, corresponding to weight loss of 2.2, 2.1, and 2.1 % respectively. The second stage reveal a weight loss of 6.2 % which corresponds to the loss of one water molecule, and the third stage shows a weight loss of 6.1 % which approximately corresponds to the loss of one water molecule yielding SrSnO<sub>3</sub>. The bottom left inset of Fig. 1(a) shows the differential scanning calorimetry (DSC) of the dried gel product (confirmed as SrSn(OH)<sub>6</sub> by thermogravimetry analysis). The Phase changes observed in DSC are in accordance with the weight loss steps observed in thermogravimetric analysis (TGA). There is no weight loss corresponding to CTAB as it was removed through multiple rinsing cycles with ethanol and has been shown in Section 3.2. The top right inset of Fig. 1(a) shows the X-ray diffraction (XRD) pattern of the above powder obtained by the heating of the gel product (formed through wet chemistry reaction) at 80 °C for 4 h. It reveals diffraction peaks

at  $2\theta$  values of 20.06, 25.43, 32.83, 36.97, 50.76, 53.65, 56.90, 60.37 and 65.56° corresponding to Bragg reflection planes (301), (400), (501),(314), (712), (713), (641), (008) and (626), respectively of strontium tin hydroxide ( $\text{SrSn}(\text{OH})_6$ ) with hexagonal type-structure. The lattice constant values are found to be 'a' = 16.18 and 'c' = 12.19 Å, and are in good agreement with the standard data (JCPDS # 09-0086).

The X-ray diffraction patterns of Fe (0, 2 and 4 at. %) doped  $\text{SrSnO}_3$  nanoparticles are shown in Fig. 1(b). The diffraction peaks of pristine  $\text{SrSnO}_3$  are observed at  $2\theta$  values of 22.1°, 31.33°, 44.8°, 55.7°, 65.3° and 74.2° corresponding to the Bragg planes (110), (200), (220), 312), (400) and (332) respectively. The planes indexed according JCPDS No. 77-1798, indicate the formation of highly crystalline orthorhombic phase of  $\text{SrSnO}_3$ . The lattice constant values of pristine  $\text{SrSnO}_3$  are calculated as  $a = 5.7$  Å,  $b = 5.7$  Å and  $c = 8.09$  Å. A slight shift in the diffraction peaks towards higher  $2\theta$  values is observed with the incorporation of  $\text{Fe}^{3+}$  in the host lattice at the  $\text{Sn}^{4+}$  site. The ionic radius of  $\text{Fe}^{3+}$  (0.64) is slightly smaller than the ionic radius of  $\text{Sn}^{4+}$  (0.69), therefore, the substitution of  $\text{Fe}^{3+}$  at the  $\text{Sn}^{4+}$  site results in the lattice contraction.

The surface morphology of synthesized perovskite structured strontium stannate nanoparticles have been studied by using high resolution transmission electron microscopy (HRTEM). The TEM images of pristine and Fe(4 at.%) doped strontium stannate nanoparticles are shown in Fig 2(a) I and 2(b) I, respectively. The TEM images clearly shows the formation of nanoparticles with particle size of about 20 nm. The HRTEM images of pristine and Fe(4 at.%) doped strontium stannate nanoparticles are shown in Fig 2(a) II and 2(b) II respectively. The measured d-spacing is about 0.288 nm which corresponds to (200) reflection of the orthorhombic phase. The inset of Fig. 2(a) II and 2(b) II shows the selected area electron diffraction patterns of the single crystal and the reflections are indexed, which are in accordance with X-ray diffraction results shown in Fig.1(b). The elemental mapping of Sr, Sn and O which are constituent elements in strontium stannate nanoparticles are shown in Fig. 2(a) III, IV and V respectively and Fig. 2(b) III, IV, V and VI shows the elemental mapping of Sr, Sn, Fe and O of Fe(4 at.%) doped strontium stannate nanoparticles. The corresponding EDS spectra of pristine and Fe(4 at.%) doped strontium stannate nanoparticles are shown in Fig. 2(a) VI and 2(b) VII respectively, which clearly shows that the final compound is composed of constituent elements such as Sr, Sn, O and Fe respective of their composition and no other impurity was detected. The atomic

composition and chemical nature of the surface of pristine and Fe (2 and 4 at %) doped SrSnO<sub>3</sub> nanoparticles were investigated by using X-ray photoelectron spectroscopy (XPS). Fig. 3(a-d) shows the high resolution XPS spectra of Sn 3d, Sr 3d, O 1s and Fe 2p, respectively. The Fig. 3(a) shows the high resolution spectra of O 1s for pristine and Fe (2 and 4 at. %) doped SrSnO<sub>3</sub> nanoparticles, which consist of two peaks at 531.8 and 533.3 eV. The first one corresponds to the O 1s, which is assigned to the SrSnO<sub>3</sub> host lattice and second peak at 533.3 eV corresponds to the hydrated oxide species in the samples. Fig. 3(b) shows the Sn 3d photoelectron peak for pristine and Fe(2 and 4 at. %) doped SrSnO<sub>3</sub> nanoparticles. The Sn 3d is splitted into a doublet. The two peaks observed at 484.8 and 493.2 eV corresponds to the Sn 3d<sub>5/2</sub> and Sn 3d<sub>3/2</sub>, respectively have an energy separation of 8.37 eV which is similar to that of Sn 3d (8.5) in SnO<sub>2</sub> [23] confirming the chemical state of Sn at the surface as +4. The FWHM values are observed to decrease with increase in Fe<sup>3+</sup> concentration which depicts the incorporation of Fe in the lattice at the desired Sn site. Fig. 3(c) shows the high resolution XPS spectra of Sr 3d photoelectron peak for pristine and Fe(2 and 4 at. %) doped SrSnO<sub>3</sub> nanoparticles, which is splitted into two peaks with binding energy 135.5 and 133.8 eV corresponding to Sr 3d<sub>3</sub> and Sr 3d<sub>5</sub>, respectively. Fig. 3(d) shows the high resolution XPS spectra of for Fe(2 and 4 at. %) doped SrSnO<sub>3</sub> nanoparticles. The Fe 2p peak was observed at 710.6 eV, which is assigned to Fe 2p<sub>1/2</sub> with Fe showing +3 oxidation state.

### 3.2 Optical characterization

Fig. 4(a) shows the Raman spectra of pristine and Fe<sup>3+</sup> (2 and 4 at %) doped SrSnO<sub>3</sub> nanoparticles. X-ray diffraction studies in Section 3.1 indicated that there is no change in the orthorhombic structure with incorporation of Fe<sup>3+</sup> in the lattice. The SrSnO<sub>3</sub> is of orthorhombic structure with the point group D<sub>2h</sub> and space group Pbnm (D<sub>162h</sub>) [23]. The Raman active modes for the Pbnm space symmetry are  $\Gamma_{\text{Raman}} = 7A_g + 5B_{1g} + 7B_{2g} + 5B_{3g}$  [24]. In the Raman spectra of the pristine and Fe<sup>3+</sup> (2 and 4 at %) doped SrSnO<sub>3</sub> perovskite, the bands at 166, 220, 256, 306, 404, 452, 561, 640, 706 cm<sup>-1</sup> are observed. The sharp peak observed around 220 cm<sup>-1</sup> is attributed to A<sub>g</sub> mode corresponding to Sn-O-Sn bond and the peak at 256 cm<sup>-1</sup> is associated with O-Sn-O bond [25]. The peak observed around 306 cm<sup>-1</sup> is due to the B<sub>2g</sub> mode corresponding to O-Sn-O bond. The bands at 306 and 404 cm<sup>-1</sup> are related to the SnO<sub>3</sub> torsional mode and the peak at 561 cm<sup>-1</sup> is related to the Sn-O stretching. The Raman peaks of corresponding wave

number are red shifted with the increase in the  $\text{Fe}^{3+}$  content in the lattice which is possibly the consequence of the increase in the particle size and effective bond length change due to reduced Coulomb force by  $\text{Fe}^{3+}$  in comparison to  $\text{Sn}^{4+}$ . The inset of Fig. 4(a) shows the Fourier transform infrared (FTIR) spectra of pristine and Fe(2 and 4 at.%) doped  $\text{SrSnO}_3$  nanoparticles. The peak observed around  $3452\text{ cm}^{-1}$  and  $1634\text{ cm}^{-1}$  represents the O-H stretching and O-H bending vibration of water molecules adsorbed on the surface of as-synthesised nanoparticles [26]. The peaks observed around  $651$  and  $544\text{ cm}^{-1}$  corresponds to the O-Sn-O bridging and Sn-OH terminal bonds [27]. The peak centered around  $1496\text{ cm}^{-1}$  corresponds to the asymmetric stretching vibration of Sn-OH bonds [28] and the peak observed around  $930\text{ cm}^{-1}$  was attributed to the vibration of carbonyl groups [29]. Further, Gökce et al. [30] theoretically calculated the vibration frequencies of the CTAB molecule using ab initio Hartree-Fock and Density Functional Theory, and compared with experimental findings. In present study, the FTIR absorption spectra (inset Fig. 4 (a)) together with Raman Spectra (Fig. 4(b)) do not exhibit any signature of CTAB presence.

The top left corner inset (I) of Fig. 4(b) shows the absorption spectra of pristine and  $\text{Fe}^{3+}$  doped  $\text{SrSnO}_3$  nanoparticles. These show the strong absorption in the UV region. The optical absorption edge in pristine  $\text{SrSnO}_3$  is observed around 290 nm, and found redshifted with increase in the doping concentration. The band gap values of as-synthesized samples were estimated from diffuse reflectance spectra by plotting the square of multiple of Kumbelka-Munk ( $F(R)$ ) function with the square of energy ( $h\nu$ ) versus  $h\nu$ , which is shown in the Fig 4(b). The extrapolated linear part of the curve at  $F(R)^2 = 0$  gives the band gap of the as synthesized samples (Fig. 4(b)-I). The band gap values of  $\text{SrSnO}_3$  nanoparticles are found to be 4.17, 3.81 and 3.51 eV for the Fe content of 0, 2 and 4 at.%, respectively. The incorporation of  $\text{Fe}^{3+}$  in the host lattice results in the increase in the particle size, and therefore, the decrease trend in the band gap is observed. Also, in  $\text{SrSnO}_3$ , the  $\text{Sn}^{4+}$  ions are in octahedral symmetry, and  $3d^5$  spin states of  $\text{Fe}^{3+}$  splits into two degenerate  $e_g$  and three degenerate  $t_{2g}$  orbitals. Thus incorporation of  $\text{Fe}^{3+}$  in the lattice results in the formation of intermittent energy states in the band gap region of  $\text{SrSnO}_3$ , which in turn results in the reduction of band gap. The bottom right corner inset (II) of Fig. 4 (b) shows the room temperature photoluminescence spectra of pristine and  $\text{Fe}^{3+}$  doped (2 and 4 at. %)  $\text{SrSnO}_3$  nanoparticles recorded at an excitation wavelength of 290 nm. The two intense peaks were observed at a wavelength of 360 and 470 nm for pristine  $\text{SrSnO}_3$  and a redshift was

observed for the Fe (2 and 4 at. %) doped samples. The band gap energy of these peaks observed at 360 nm corresponds to the band gap values calculated from the absorption spectrum corresponding to the direct allowed transition between O2p and Sn 5s energy levels [31]. The  $\text{Sn}^{+4}$  has higher charge than  $\text{Fe}^{3+}$  ions and as a consequence of charge balance there will be increase in the oxygen vacancies in the host lattice as a result of that the reduction in the intensity of PL peaks is observed. The other peak observed at 470 nm corresponds to the emission occurred from the various defect energy levels which were in the band gap region. Population of these defect levels was found to increase with increase in Fe content.

### 3.3 Dielectric properties

The variation of relative permittivity ( $\epsilon'$ ) as a function of frequency at various temperatures for pristine and Fe(2 and 4 at. %) containing  $\text{SrSnO}_3$  samples obtained by the pelletization of respective nanopowders and subsequent sintering at 923 K for 2 h are depicted in Fig. 5- a, b and c, respectively. The two distinguishable regions are clearly observed: (i) the plateau region at higher frequency and (ii) the dispersive nature at the lower frequency. The  $\epsilon'$  decreases with increase in frequency, which is due to the fact that at lower frequency  $\epsilon'$  varies with deformational and relaxation polarization mechanisms. The deformational polarization mechanism depends on the displacement of charge carriers whereas relaxation mechanism depends on the orientation of charge carriers in the influence of an external electric field, however, at higher frequency there will be decrease in the orientation polarization, as the molecular dipoles takes more time to change their orientation under the influence of external electric field. The  $\epsilon'$  is found to increase with increase in the ferric ion content. From Section 3.2 it was observed that the band gap decreases with increase in the doping concentration. The dielectric constant increases with decrease in the band gap, this can be explained by using electronic polarizability phenomenon. If the band gap decreases further, the electron in the valence band tend to move to the conduction band more easily and the energy gap between the bonding and anti-bonding states decreases, as a result, the corresponding wave function can be easily altered by varying the external electric field. Therefore, the dielectric constant increases as the electron polarizability increases [32]. The insets of Fig. 5 a, b and c shows the variation of dielectric loss tangent ( $\tan \delta$ ) as a function of frequency at various temperatures. The peaks are observed in the plot of loss tangent as a function of frequency, which indicates the presence of

relaxation mechanism. The relaxation peaks are shifted towards the higher frequency indicating that the charge carriers inside the sample are thermally activated. The relaxation time is found to decrease with temperature and is tend to increase with increase in ferric ion concentration as the charge carriers get increased, and it is difficult for the dipoles to align into the initial position, which is tend to enhance the relaxation time. The variation of relaxation time with temperature and Fe content is shown in Fig 5-d.

### 3.4. Temperature and frequency dependence on ac conductivity

Fig. 6 a, b and c shows the variation of ac conductivity as a function of frequency at different temperatures. The ac conductivity as a function of frequency  $\sigma(\omega)$  is given by the relation,  $\sigma(\omega) = \omega \epsilon_0 \epsilon' \tan(\delta)$  [33], where  $\epsilon_0$  is the permittivity of free space,  $\epsilon'$  is the relative permittivity and  $\tan(\delta)$  is the dielectric loss tangent. The variation of ac conductivity with frequency  $\sigma(\omega)$  follows the Jonscher power law [34],  $\sigma(\omega) = \sigma_0 + A\omega^n$ , where  $\sigma_0$  is the dc conductivity obtained by extrapolating the conductivity to the lowest angular frequency, A is the pre-exponential factor and n represents the degree of interaction between the mobile ions and the surrounding ions in the lattice [35]. It is observed from the Fig. 6- a, b and c that the ac conductivity increases with frequency at different temperatures. Fig. 6-d shows the variation of logarithm of ac conductivity with the reciprocal of temperature at a frequency of 1 KHz. The ac conductivity ( $\sigma$ ) of pristine and Fe (2 and 4 at %) doped SrSnO<sub>3</sub> nanoparticles at room temperature (310 K) is found to be  $3.23 \times 10^{-8}$ ,  $3.98 \times 10^{-8}$  and  $4.47 \times 10^{-8} \Omega^{-1} \text{cm}^{-1}$  respectively. Obviously, conductivity increases with doping concentration, as the charge carriers get enhanced in the band region of SrSnO<sub>3</sub>. The activation energy ( $E_a$ ) of pristine and Fe (2 and 4 at %) doped SrSnO<sub>3</sub> is calculated using the Arrhenius relation. The activation energy is found to be 0.22 ,0.34 and 0.42 eV for the pristine and Fe (2 and 4 at %) doped SrSnO<sub>3</sub> nanoparticles, respectively. The hopping frequency has been estimated by Jonscher power law proposed by Almond-West and given by expression  $\sigma_{ac} = \sigma_{dc} [1 + (\omega/\omega_h)^s]$  [36,37], where  $\omega_h$  is the hopping frequency of the charge carriers. Fig. 6-d shows the variation of logarithm of hopping frequency ( $\omega_h$ ) with reciprocal of temperature . The temperature dependent hopping frequency ( $\omega_h$ ) is known to obey Arrhenius relation as,  $\omega_h = \omega_0 e^{(-E_w/KT)}$ , where  $\omega_0$  is the pre exponential factor, and  $E_w$  is the hopping activation energy. The hopping activation energy is found to be 0.25, 0.31 and 0.41 eV for pristine and Fe (2 and 4 at %) doped SrSnO<sub>3</sub> nanoparticles, respectively. The activation energy and hopping activation

energy is found to be approximately same, which conveys that the mobility of charge carriers in the lattice may be due to the hopping mechanism.

#### **4. Conclusions**

The composition  $\text{SrSn}_{1-x}\text{Fe}_x\text{O}_3$  has been synthesized successfully by wet chemical route. X-ray diffraction patterns revealed the formation of orthorhombic phase  $\text{SrSnO}_3$  nanoparticles. HRTEM images confirm the formation of nanoparticles having particle size around 20 nm. It has been observed that Fe substitution on Sn site has a considerable effect on the dielectric behavior of the material. The relative permittivity as a function of frequency at different temperatures was found to increase with temperature and Fe content. The relaxation time was found to decrease with temperature and increase with Fe content. The ac conductivity values and activation energies were found to increase with increase in the Fe content.

#### **Acknowledgement**

This work was supported by SERB, Government of India (SERB/F/1769/2013-2014).

## References

- [1] W.F. Zhang, J. Tang and J. Ye, *Chem.Phys.Lett.*, 2006, **418**, 174–178.
- [2] S. Ouni, S. Nouri, H. Khemakhem and R.B. Hassen, *Mater.Res.Bull.*, 2014, **51**, 136-140.
- [3] Y. Li, H. Zhang, B. Guo, M. Wei, *Electrochim.Acta.*, 2012, **70**, 313-317.
- [4] G. Prathiba, S. Venkatesh and N.H. Kumar, *Solid.State.Commun.*, 2010, **150**, 1436-1438.
- [5] Q.Z. Liu, H.F. Wang, F. Chen and W.J. Wu, *Appl.Phys.*, 2008, **103**, 093709.
- [6] G. Prathiba, S. Venkatesh, K.K. Bharathi and N.H. Kumar, *J.Appl.Phys.*, 2011, **109**, 07C320.
- [7] A.M. Azad, L.L.W. Shyam, M.A. Alim, *J.Mater.Sci.*, 1999, **34**, 1175-1187.
- [8] C.W. Lee, D.W. Kim, I.S. Cho, S. Park, S.S. Shin, A.W. Seo and K.S. Hong, *Int.J.Hydrogen.Energy*, 2012, **37**, 10557-10563.
- [9] A.L. Goodwin, A.T. Redfern, M.T. Dove, D.A. Keen and M.G. Tucker, *Phys.Rev.B.*, 2007, **76**, 174114.
- [10] A.Kumar, R.N.P.Choudary, B.P.Singh, A.K.Thakur, *Ceramic International*, 2006, **32**, 73-83.
- [11] A.M.Azad, T.Y.Pang and M.A.Alim, *Active and Passive Elec.Comp.*, 2003, **26**, 151-166.
- [12] J.Bohnemann, R.Libanori, M.L.Moreira, E.Longo, *Chemical Engineering Journal*, 2009, **155**, 905-909.
- [13] D.K. Patel, B. Rajeswari, V. Sudarsan, R.K. Vatsa, R.M. Kadam and S.K. Kulshreshtha, *Dalton.Trans.*, 2012, **41**, 12023.
- [14] S. Ouni, S. Nouri, J. Rohlicek, R.B. Hassen, *J.Solid.State. Chem.*, 2012, **192**, 132-138.
- [15] W. Zhang, J. Tang and J. Ye, *J Mater Res.*, 2007, **22**, 1859-71.
- [16] C. Li, Y. Zhu, S. Fang, H. Wang, Y. Gui, L. Bi and R.Chen, *J.Phys.Chem.Solids*, 2011, **72**, 869-874.
- [17] X. Wang and S. Zhang, *Mater.Sci and Engg: B*, 2001, **86**, 29-33.
- [18] S. Soleimanpour and F. Kanjouri, *Physica.B*, 2014, **432**, 16-20.
- [19] X. Han, X. Li, X. Long, H. He and Y. Cao, *J.Mater.Chem*, 2009, **19**, 6132-6136.
- [20] T. Endo, T. Masuda, H. Takizawa and J. Shimada, *J.Mater.Sci.Lett.*, 1992, **11**, 1330-1332.
- [21] S. Singh, P. Singh, O. Prakash, D. Kumar, *Adv. Apl.Ceramics*, 2007, **106**, 5.

- [22] O. Pakash, K.D. Mandal, C.C. Christopher and M.S. Sastry, *J.Mater.Sci.Lett* 1996, **31**, 4705-4708.
- [23] G.L. Lucena, A.S. Maina, A.G. Souza and I.M.G. Santos, *J.Therm.Anal.Calorim.*, 2014 **115**, 137-144.
- [24] M. Glerup, K.S. Knight and F.W. Polusen, *Mater.Res.Bull.*, 2005, **40**, 507-520.
- [25] E. Moreira, J.M. Henriques, D.L. Azevedo, E.W.S. Caetano, V.N. Freire and E.L. Albuquerque, *J.Solid.State.Chem.*, 2011, **184**, 921-928.
- [26] H. Cui, Y. Lui, W. Ren, M. Wang and Y. Zhao, *Nanotechnology*, 2013, **24**, 345602.
- [27] A. Kumar and J. Kumar, *J.Solid.State.Commun*, 2008, **147**, 405-408.
- [28] H. Guo, R. Mao, D. Tian, W. Wang, D. Zhao, X. Yang and S. Wang, *J.Mater.Chem.A*, 2013, **1**, 3652.
- [29] M.Tarrida, H.Larguem, M.Mardon, *Phys Chem Minerals*,2009,**36**,403-413.
- [30] H. Gökce, H and S. Bahçeli, *Optics and Spectroscopy*, 2013, *115*(5), 632-644.
- [31] D. Chen and J. Ye, *Chem.Mater*, 2007, **19**, 4585-4591.
- [32] S. Das, D.Y. Kim, C.M. Choi and Y.B. Hahn, *Mater.Res.Bull*, 2013, **46**, 609-614.
- [33] C. Sevik and C. Bulutay, *Phys.Rev.B*, 2006, **74**, 193-201.
- [34] S.Kumar and K.B.R. Varma, *Current.Apl.Phys.*, 2011, **11**, 203-210.
- [35] A.K. Jonscher, *Nature* 1977, **267**, 673.
- [36] S. Kumar and K.B.R. Varma, *Solid State Commun.*, 2008, **146**, 137-142.
- [37] D.P. Almond and A.R. West, *Nature*, 1983, **306**, 455.

### Figure captions

**Fig. 1(a)** (Color online) the thermo gravimetric analysis of the powder obtained by the heating of the gel product at 80 °C for 4 h formed through wet chemistry reaction, and drying subsequently at 100 °C for 2 h; bottom left inset shows the Differential thermal analysis of SrSn(OH)<sub>6</sub> nanoparticles, top right inset shows X-ray diffraction pattern of the SrSn(OH)<sub>6</sub> nanoparticles, and (b) X-ray diffraction pattern of SrSnO<sub>3</sub> nanoparticles with Fe content of 0, 2 and 4 at. %; inset shows the details of the peak ( $2\theta = 31.33$ ).

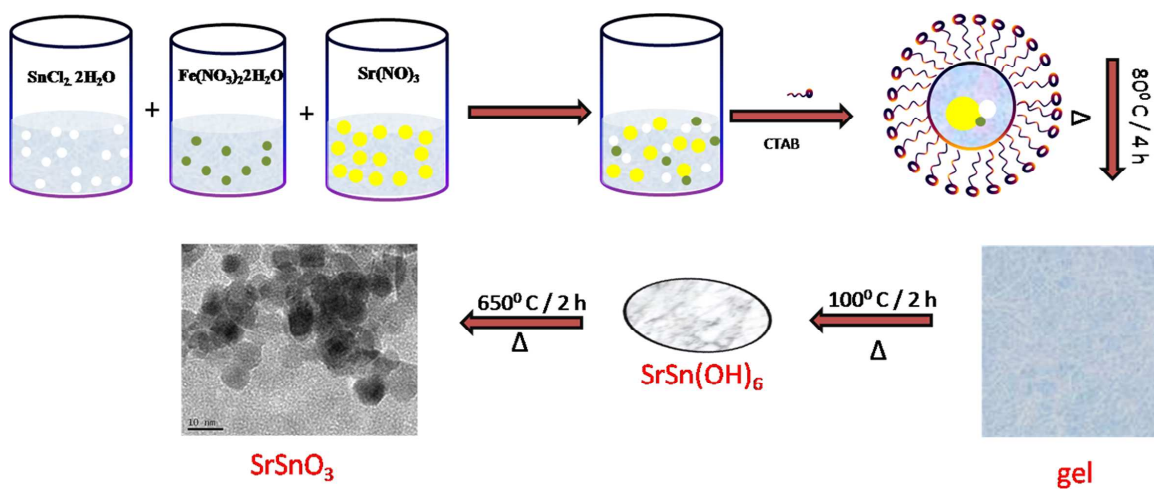
**Fig. 2** (a) (I) (Color online) HRTEM image, (II) Lattice fringe pattern, inset shows the SAED pattern, (III-V) Elemental mapping Sr, Sn and O, and (VI) EDS spectra of pristine SrSnO<sub>3</sub> nanoparticles. (b) (I) HRTEM image, (II) Lattice fringe pattern, inset shows the SAED pattern, (III-V) Elemental mapping Sr, Sn, O and Fe and (VI) EDS spectra of Fe (3 at %) doped SrSnO<sub>3</sub> nanoparticles.

**Fig. 3(a-d)** (Color online) High resolution X-ray photoelectron spectroscopy spectra of Sr 3d, Sn 3d, O 1s and Fe 2p orbitals.

**Fig. 4(a)** (Color online) Raman spectra of pristine and Fe doped SrSnO<sub>3</sub> nanoparticles; inset shows the Fourier transform infra red spectra of pristine and Fe doped SrSnO<sub>3</sub> nanoparticles (b) Tauc's plots for band gap estimation for pristine and Fe doped SrSnO<sub>3</sub> nanoparticles.; top left corner inset (I) shows the absorption spectra, and the bottom left corner inset (II) shows the photoluminescence spectra for the pristine and Fe doped SrSnO<sub>3</sub> nanoparticles

**Fig. 5- a-c** (Color online) Frequency dependent dielectric constant ( $\epsilon'$ ) and inset shows the variation of loss tangent of pristine and Fe (2 and 4 at.%) doped SrSnO<sub>3</sub> nanoparticles at different temperatures, and (d) The variation of relaxation time with temperature and Fe content.

**Fig. 6- a-c** (Color online) Frequency dependent ac conductivity and (d) shows the variation of ac conductivity and inset shows the variation of hopping frequency of pristine and Fe (2 and 4 at.%) doped SrSnO<sub>3</sub> nanoparticles at different temperatures.



**Scheme 1:** Showing synthesis of SrSnO<sub>3</sub> nanoparticles

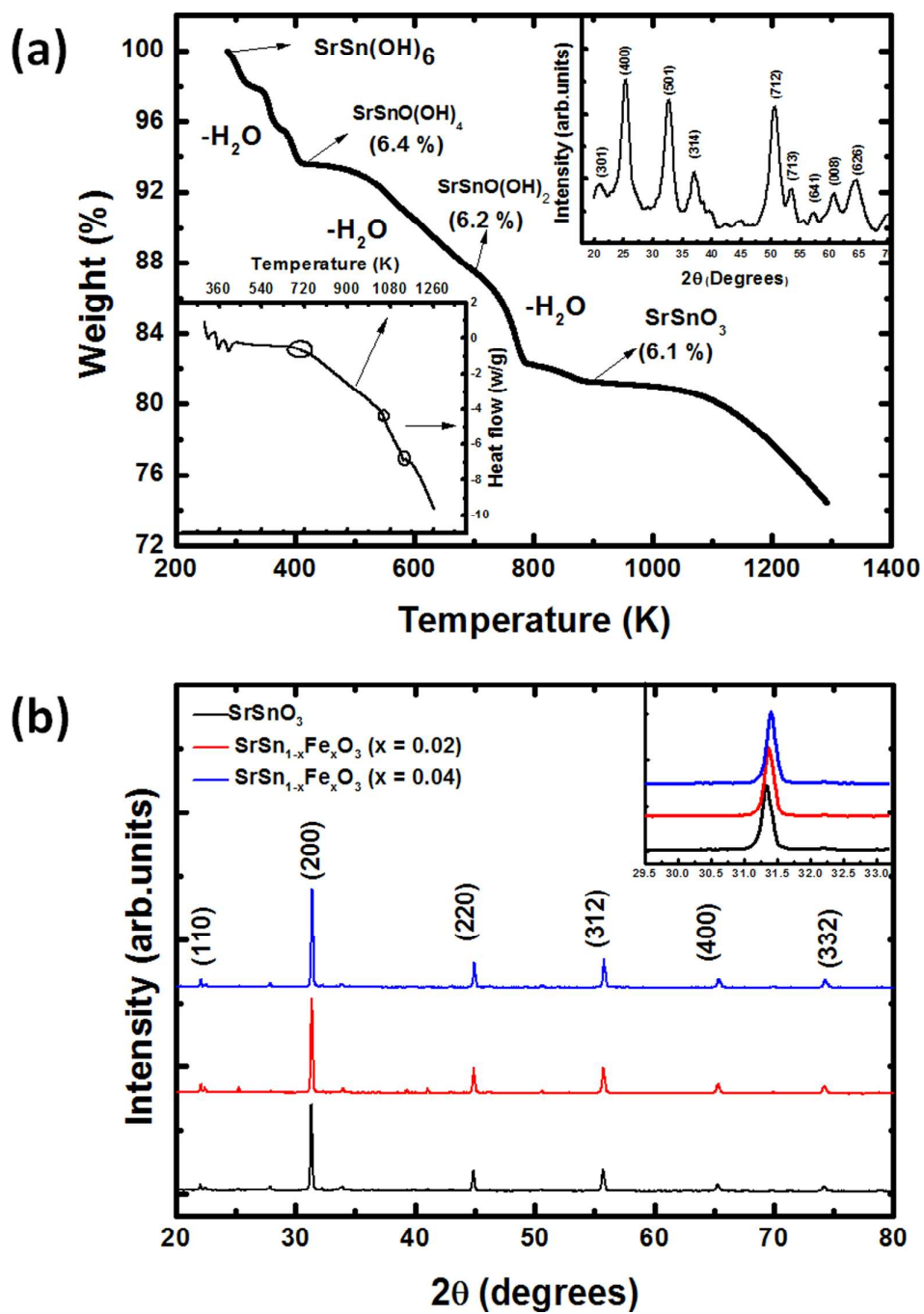


FIG. 1

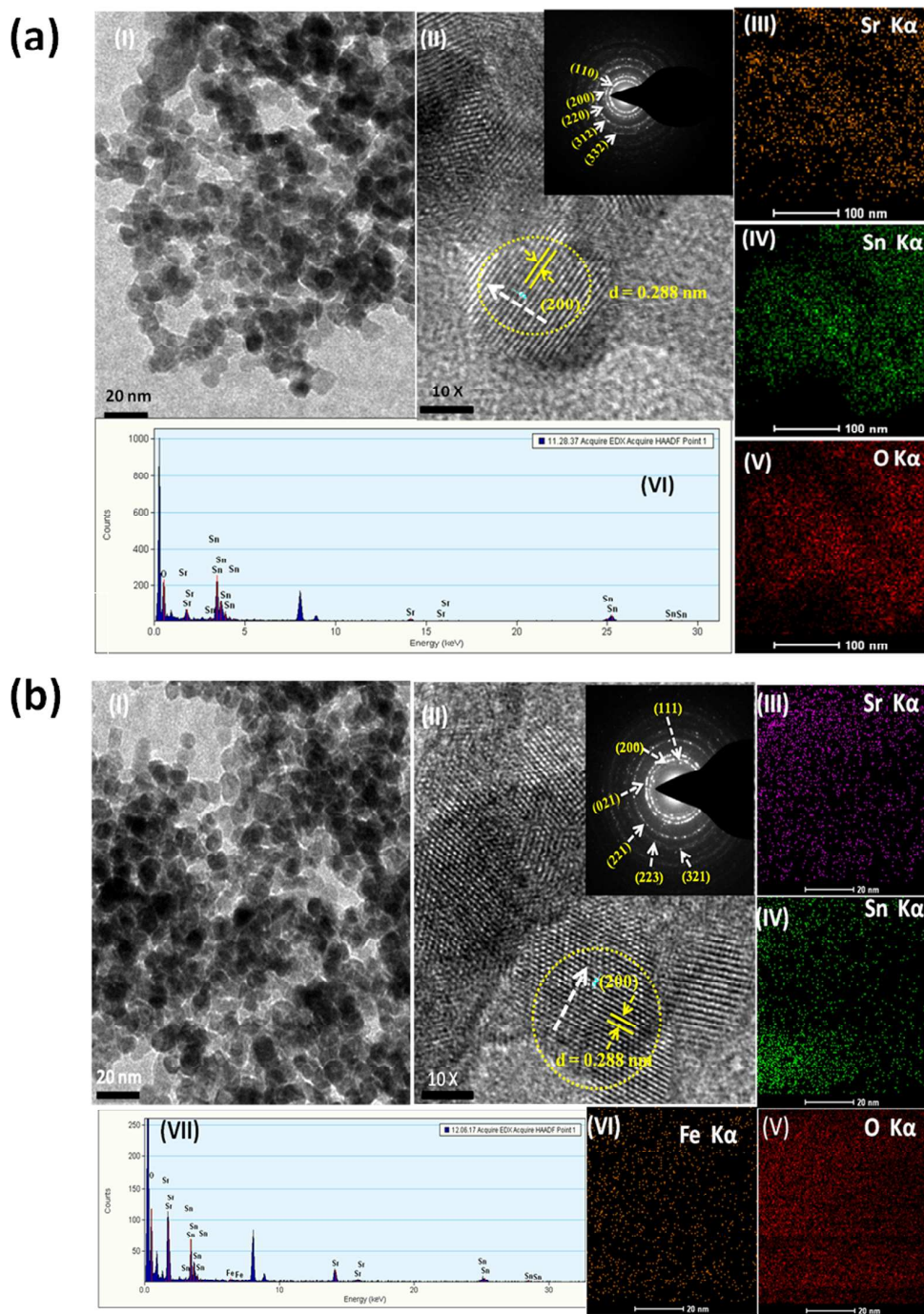


FIG. 2

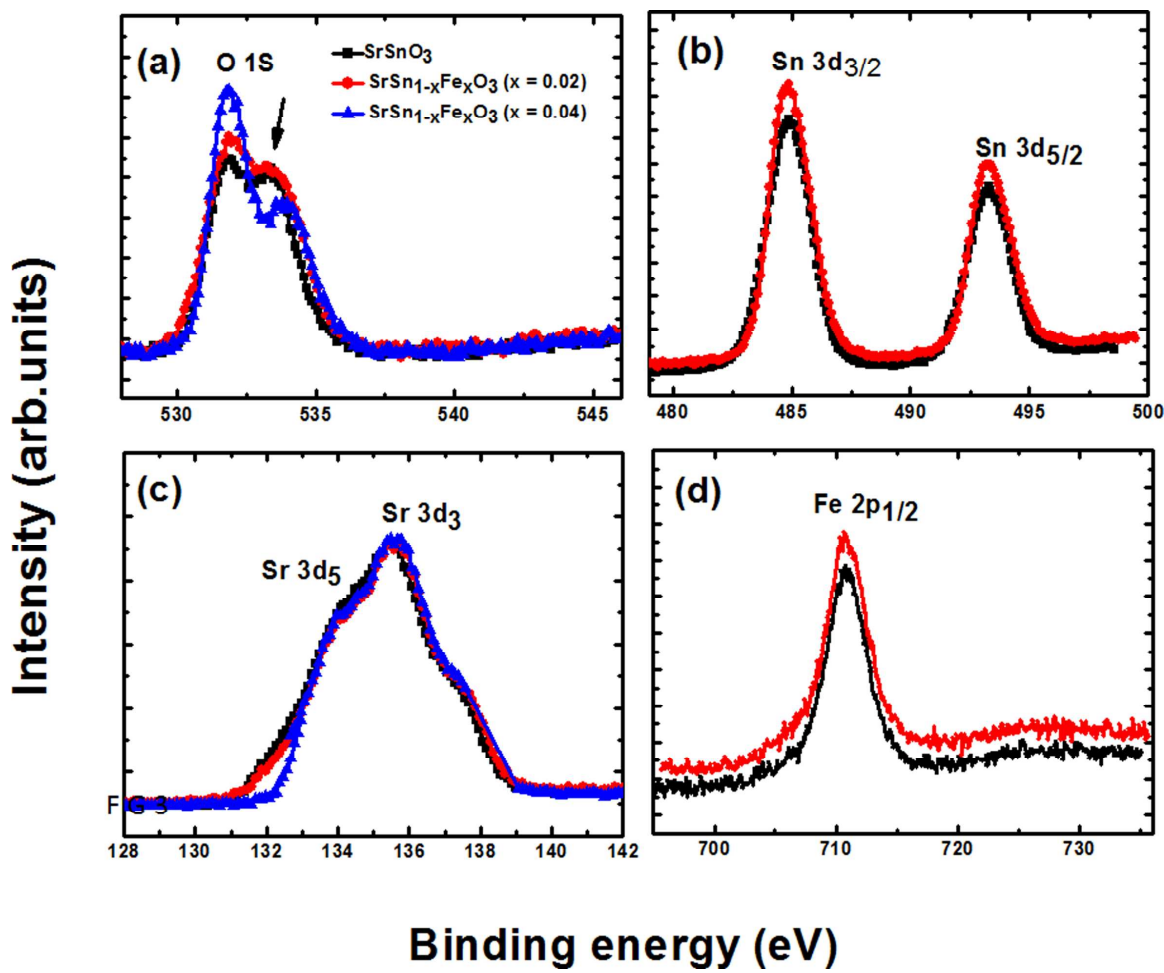


FIG. 3

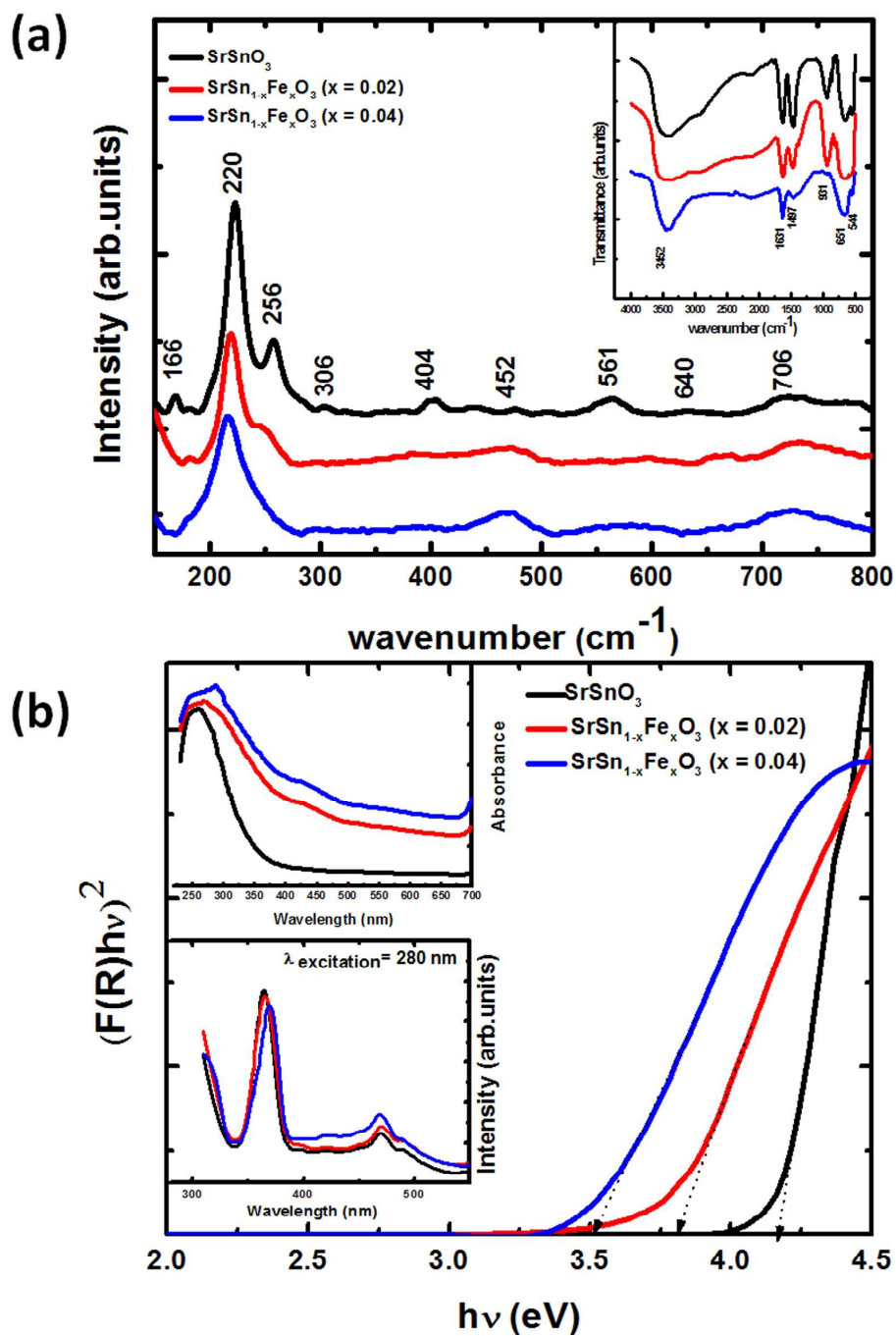


FIG. 4

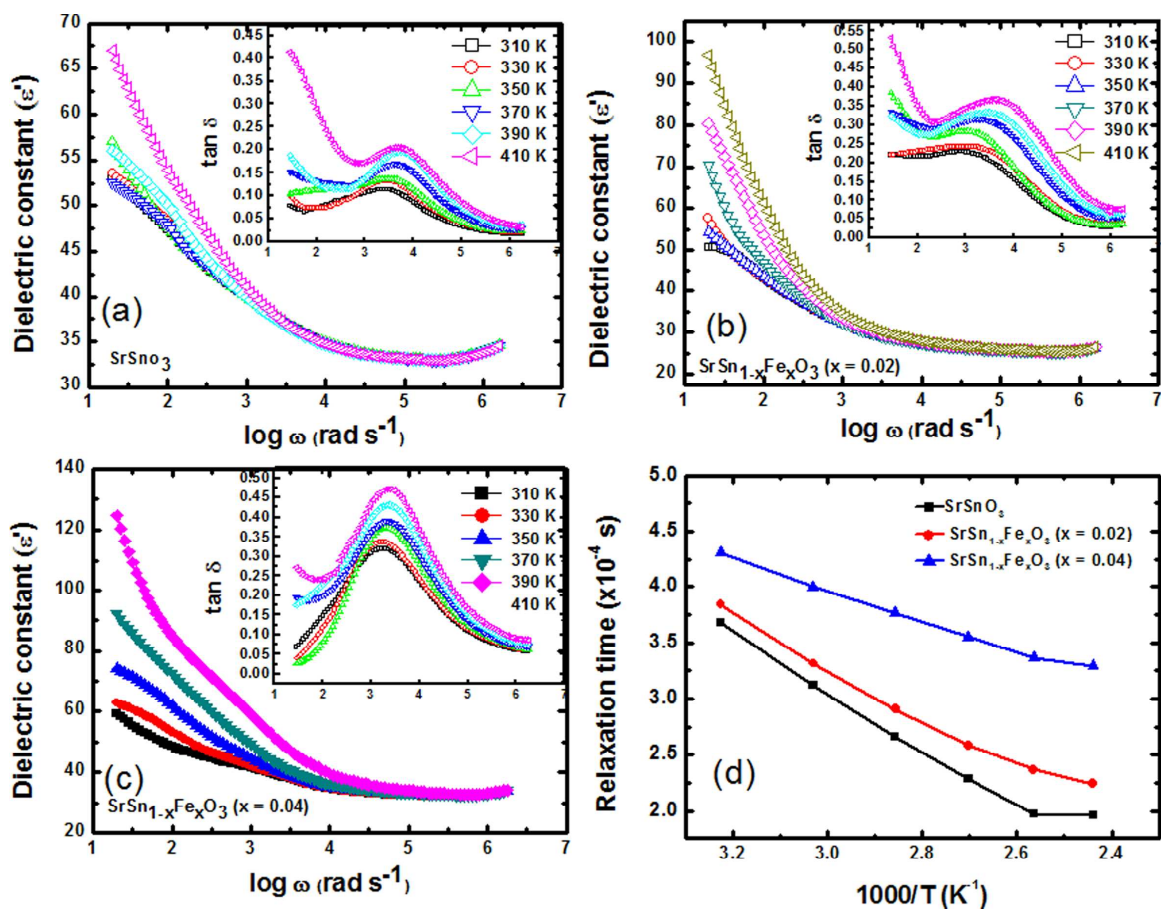


FIG. 5

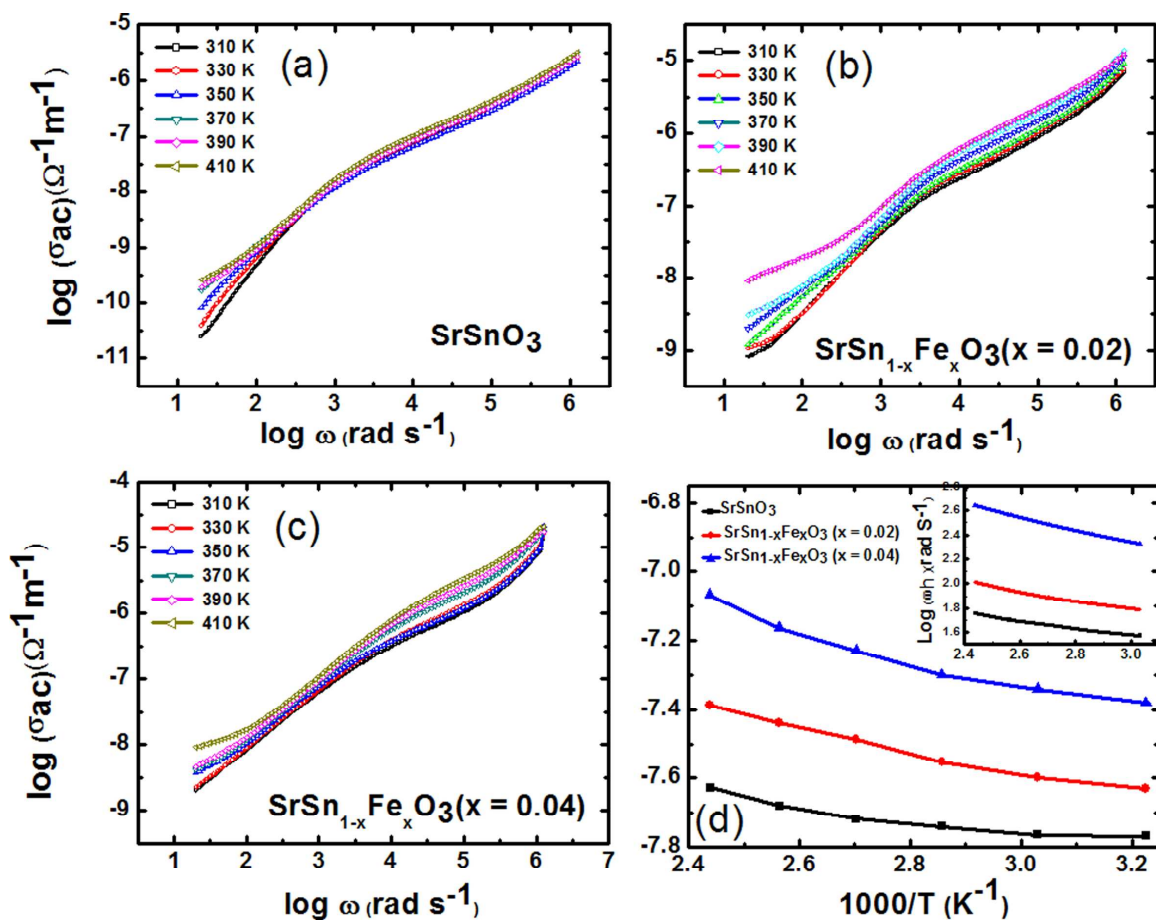


FIG. 6